[22] H.S. Cho, K. Mason, K.X. Ramyar, A.M. Stanley, S.B. Gabelli, D.W. Denney Jr., D.J. Leahy, Structure of the extracellular region of HER2 alone and in complex with the Herceptin Fab, Nature 13 (2003) 756–760.
[23] X. Meng, M. Samso, M.-P. Koonce, A flexible linkage between the dynein motor and its cargo, J. Mol. Biol. 357 (2006) 701–706.
[24] S.-A. Burgess, M.-L. Walker, H. Sakakibara, K. Oiwa, P.-J. Knight, The structure of dynein-c by negative stain electron microscopy, J. Struct. Biol. 146 (2004) 205–216.
[25] M. Samso, M. Radermacher, J. Frank, M.-P. Koonce, Structural characterization of a dynein motor domain, J. Mol. Biol. 276 (1998) 927–937.

Journal of Nanoparticle Research (2007) 9:1067–1071
DOI 10.1007/s11051-006-9186-2
© Springer 2007

Research Paper

Organic-ligand-assisted supercritical hydrothermal synthesis of titanium oxide nanocrystals leading to perfectly dispersed titanium oxide nanoparticle in organic phase

Tahereh Mousavand, Jing Zhang, Satoshi Ohara, Mitsuo Umetsu, Takashi Naka and Tadafumi Adschiri*
*Institute of Multidisciplinary Research for Advanced Materials, Tohoku University, 2-1-1 Katahira, Aoba-ku, Sendai, 980-8577, Japan; *Author for correspondence (Tel.: +81-22-2175629; Fax: +81-22-2175631; E-mail: ajiri@tagen.tohoku.ac.jp)*

Received 3 March 2006; accepted in revised form 21 October 2006

Key words: dispersion, metal oxide, mixing, nanoparticle, supercritical hydrothermal synthesis

Abstract

Titanium oxide (TiO_2) nanocyrstals which are perfectly dispersed in organic solvents are synthesized by organic-ligand-assisted supercritical hydrothermal synthesis. The addition of hexaldehyde to the supercritical hydrothermal synthesis of TiO_2 leads to the *in-situ* surface modification, which enables the synthsized TiO_2 nanocrystals to be perfectly dispersed in iso-octane because of its hydrophobic nature. Further, the one-pot synthesis of hybrid materials results in the significant reduction of the particles size, probably due to the capping effect of hexaldehyde to suppress the particles growth.

Introduction

Metal oxide nanoparticles have been extensively investigated due to their present successful application and the foresight of their use in various fields of electronics, catalysis, pharmaceutics, energy storage and medical applications. Physical and chemical properties of the nanoparticles are varied by changing the size and morphology of the nanoparticles. The organization of these nanoparticles into functional systems has been expected as the expression of unique electric, photonic, and magnetic functions. For organizing the inorganic nanostructures, hybridization with organic materials is one of the attracting methods because various self-fabrications controlled by molecular structure can be utilized (Li et al., 2003). The surface on metal oxide particle is generally so hydrophilic by the presence of hydroxyl groups that the metal oxide particles are not well dispersed in an organic phase. In addition, the extremely high surface energy of nanoparticles leads to the aggregation of the nanoparticles (Singhal et al., 1999; Sanchez et al., 2001).

In order to attain good dispersion of metal oxide nanoparticles in organic phase, the utilization of a dispersing agent or the formation of hydrophobic surface layer around the nanoparticles is necessary (Bonnemann et al., 1996; Horn & Rieger et al., 2001); however, the present methods are not always applied for metal oxide particles. Recently, we have succeeded in the synthesis of various organic–inorganic hybrid materials in supercritical water with alcohol, aldehyde, carboxylic acids, or amine as the organic ligand, and reported that the organic molecule with an aldehyde group can change the surface properties of titanium oxide (TiO_2) materials (Mousavand et al., 2006a, b).

Here, we propose an one-pot synthesis of a surface-modified TiO_2 nanoparticle in supercritical fluid for spontaneous dispersion of the particle in non-polar organic phase.

Experimental

A 0.01 M TiO_2 colloid solution (ISHIHARA SANGYO KAISHA, Ltd. (Japan), the colloid size: 30 nm) and a 0.1 ml of hexaldehyde ($CH_3(CH_2)_4CHO$) was loaded into a pressure-resistant vessel (SUS316) with 5 ml of inner volume. The reactor was heated and shaken for 10 min in an electric furnace which controlled external surface temperature of the reactors at 200°C and 400°C. During the reactions, the pressures inside the reactor were 20 MPa and 40 MPa at 200 and 400°C, respectively. A 0.01 M $Ti(SO_4)_2$ solution was also used as a starting material to conduct the experiments with the same procedure as for the TiO_2 colloid solution. The ratio of organic modifier to aqueous solution was 38:1. The products were exported from the reactor into a beaker and were purified by repeating with decantation and centrifugation in ethanol several times. The purified products were transported into a two-phase mixture of water and chloroform, or water and iso-octane, in order to observe the dispersibility of the products in the organic phase.

The products were analyzed by X-ray diffractometry (XRD), infrared spectroscopy, thermogravimetry analysis (TGA), and electron microscopy. The XRD data were measured on a Dmax γ_n X-ray diffractometer (Rigaku) with CuKα radiation. For analyzing the organic molecules contained in the products, attenuated total reflectance (ATR) Fourier transform infrared (FT-IR) spectra were measured with a FT-IR-680 plus spectrometer (Jasco, Tokyo, Japan) at a resolution of 4 cm^{-1}. TGA was performed by a Thermo Plus (Rigaku) under a constant flow of argon gas at the heating rate of 10°C min^{-1}. The size and morphology of the prodcuts were observed with a transmission electron microscopy (TEM, JEM-1200 EX II (JEOL, Ltd.)).

Results and discussion

Figure 1 shows the products obtained from the TiO_2 colloid, in the separated liquids of water and chloroform (a, b), and water and isooctane (c, d). The TiO_2 particles obtained at 200°C without hexaldehyde were dispersed in water (shown in Figure 1a), similarly to the untreated TiO_2 particles, while those heated with hexaldehyde were dispersed in a chloroform phase (shown in Figure 1b). The heat treatment with the organic molecules changes the surface property of the TiO_2 particles, and the property change implies the immobilization of the organic molecules on the TiO_2 particles. However, the surface-modified TiO_2 particles were not dispersed to the organic phase in the mixture of water and iso-octane, as well as the unmodified TiO_2 particles (shown in Figure 1c, d). The TiO_2 particles treated at 400°C with hexaldehyde showed the same result (data not shown). The amount of immobilized organic molecules on the TiO_2 particles might not be

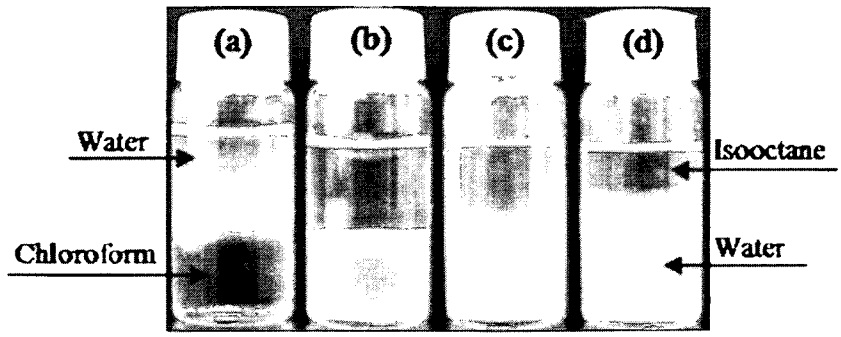

Figure 1. Dispersibility of colloidal TiO_2: (a, c) in a mixture of water and chloroform, (b, d) in a mixture of water and iso-octane. (a, c) colloidal TiO_2 treated at 200°C; (b, d) colloidal TiO_2 heated at 200°C in a mixture of water and iso-octane with hexaldehyde.

sufficient for goods dispersion in an non-polar organic solvent, nor the starting materials, TiO_2 colloid, might not have enough binding sites for the organic ligands to react.

Thus, we attempted the *in-situ* surface modification during supercritical hydrothermal synthesis of TiO_2 particles; a $Ti(SO_4)_2$ solution was heated to 200°C or 400°C in the presence of hexaldehyde with the same condition as the TiO_2 colloid experiment. The XRD patterns of the precipitated particles indicated the formation of TiO_2 anatase phase (data not shown). Figure 2 shows the dispersibility of TiO_2 particles in dispersant. The bottles contain 0.42 g of modified TiO_2 in 6.0 ml iso-octane. Although the TiO_2 particles synthesized at 200°C were dispersed only in water phase (Figure 2a), the addition of hexaldehyde in the synthesis at 400°C resulted in a well dispersion of the synthesized particles in isooctane (shown in Figure 2b). This implies more efficient immobilization of hexaldehyde on the TiO_2 nanoparticles for the *in-situ* surface modification during the supercritical hydrothermal synthesis than for post surface modification.

In order to evaluate the binding strength of the organic molecules on the synthesized TiO_2 particles, TGA was performed (shown in Figure 3). The synthesized TiO_2 particles at 200°C in the presence of hexaldehyde showed the comparable

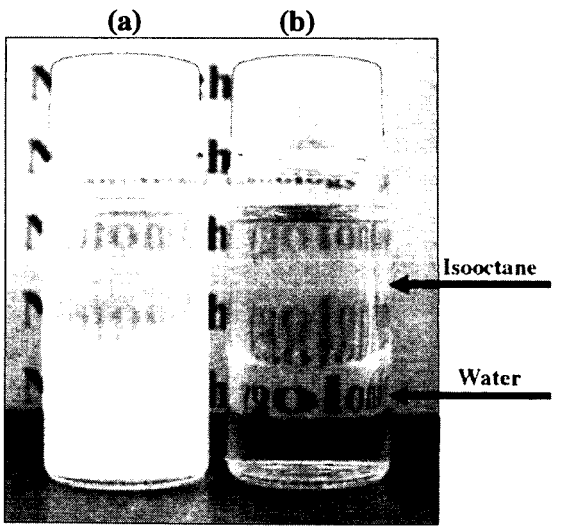

Figure 2. Dispersibility of TiO_2 nanoparticles synthesized with hexaldehyde: (a) at 200°C and (b) at 400°C, in a two-phase mixture of water and isooctane (ratio of hexaldehyde to aqueous solution is 38:1).

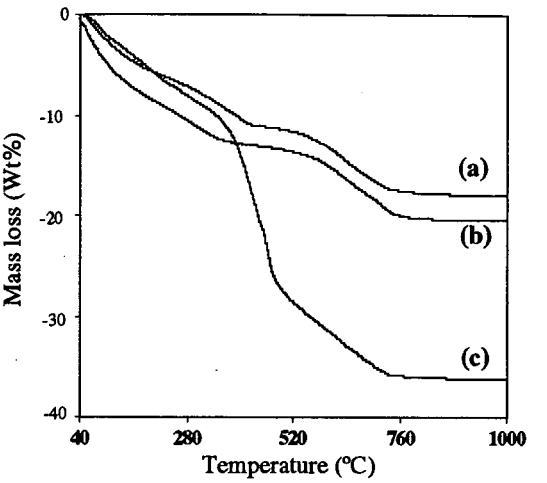

Figure 3. TGA curves of synthesized TiO_2 nanoparticles. (a) TiO_2 particles synthesized at 200°C without hexaldehyde; (b) TiO_2 particles synthesized at 200°C with hexaldehyde; (c) TiO_2 particles synthesized at 400°C with hexaldehyde.

TG curve to that of the synthesized TiO_2 particles without hexaldehyde. This result indicated that little amount of organic molecules bonded with the surface of nanoparticles. In contrast, the weight of the synthesized TiO_2 particles at 400°C with the organic molecules was drastically decreased around the 400°C. This supports the presence of organic compound only on the TiO_2 particles synthesized at 400°C. From the fact that the mass loss of the synthesized TiO_2 particles with the organic molecules was observed at high temperature, it is possible that the binding of the organic molecules on the TiO_2 particles is not physical adsorption, but rather, covalent binding. Density of organic molecule on the surface of nanoparticle was estimated from the specific surface area and the weight fraction of organic molecules on the particles. The specific surface area was estimated from the particle size (10 nm) observed by TEM, and the weight fraction was evaluated by TG analysis. Percentage of organic coverage (hexaldehyde) on the surface of nanoparticles synthesized at 400°C was evaluated to be about 70%. We analyzed the samples by FTIR and TGA for confirming the chemical bonding between organic modifier and particles surface (data not shown). FTIR analysis showed the presence of CH_2, CH_3 and C–O bonding as chemical bonds on the surface of TiO_2 nanoparticles, even after the several

times of the samples to remove physisorbed organic molecules. TGA (400°C) results showed the drastic decrease of the weight at above 300°C, which suggests decomposition of organic molecules. The physisorbed molecules which might not be washed out would be evaporated at a much lower temperature. From these two results, we concluded the chemical bonding between organic modifier and inorganic surface.

Although the detailed mechanism has not been elucidated, at the moment, we think a following reaction may occur: TiO_2 nuclei have been formed during hydrothermal synthesis, whose surface is hydroxide. When the organic species are added to the system, organic species and aqueous solution forms a homogeneous phase at the supercritical condition, and the organic molecules are chemisorbed or physisorbed on the surface of TiO_2 nuclei, which is followed by reaction (probably dehydration) to form chemical bonds.

Figure 4 shows the TEM images of the TiO_2 particles synthesized at 400°C. The synthesized TiO_2 particles without hexaldehyde used were aggregated and the size distribution was broad, ranging from several nm to 70 nm, while with the hexaldehyde, the particles were relatively dispersed on the grid and the size was in the range of several to 10 nm. It should be noted that the addition of the organic molecules resulted in the reduction of particle size and the dispersion of the particles. The immobilization of the organic molecules immediately after the nucleation of the particles probably suppressed the nuclei growth, and in addition, the formation of the organic layer also suppressed the aggregation of nanoparticles in the solution.

Supercritical hydrothermal reaction is one of the effective methods for the synthesis of highly-crystalline metal oxide materials. The high reaction rate of hydrothermal synthesis and low solubility of metal oxide in supercritical water result in the production of nanoparticles (Adschiri et al., 1992; Adschiri et al., 2001); however, nuclei growth is not completely controlled especially for the case of using a batch reactor where rapid heating of the solution cannot be achieved. Also, the perfect dispersion of the nanoparticles in an organic phase is difficult to achieve because of the high surface energy of the particles and the hydrophilic nature of the particles surface. The TiO_2 particles synthesized in this study, even by using batch reactor, were less than 10 nm in size and well dispersed in an organic phase. At the supercritical condition, the supercritical water forms a homogenous phase with organic molecules because of the lower dielectric constant of supercritical water, and dehydration occurs. Therefore, hexaldehyde might homogeneously and aggressively react with the metal hydrate, and thus, the particle growth is suppressed with a chemically bonded hydrophobic layer formed on its surface.

Conclusion

In conclusion, organic-ligand-assisted supercritical hydrothermal synthesis from $Ti(SO_4)_2$ and hexaldehyde can synthesize the organic-phase-dispersed

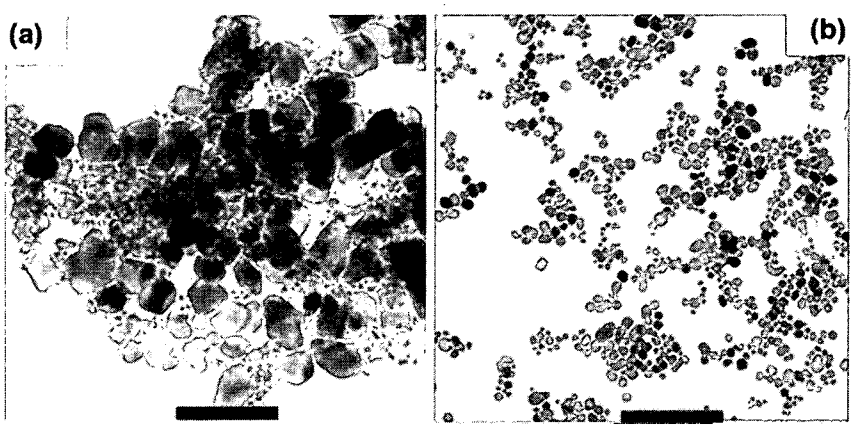

Figure 4. TEM images of TiO_2 nanoparticles synthesized at 400°C: (a) without hexaldehyde, (b) with hexaldehyde (Scale bar is 100 nm).

TiO_2 nanoparticles with chemically bonded organic molecules layer formed on their surfaces. The TEM images demonstrated that using the modifier reagent could control both the size and the aggregation of the nanoparticles; and size of nanocrystals synthesized at higher temperature was smaller. Besides, TG analysis confirmed high percentage of organic coverage on the nanoparticles surfaces synthesized at higher temperature, 400°C. The results of the dispersibility also revealed changing the surface property of the nanoparticles to hydrophobic. Therefore, the *in-situ* surface modification is very effective for making transparent dispersion in organic media. This noble synthesis method is expected to be applied for various combinations of metal oxides and organic modifiers.

Acknowledgments

This work was supported by a Scientific Research Grant from the Ministry of Education, Science, Sports, and Culture of Japan (T.A.). This research was also partly supported by the HEIWA NAKAJIMA foundation (T.A.) and by a Grant-in-Aid for the COE project, Giant Molecules and Complex Systems, 2002.

References

Adschiri T., K. Kanazawa & K. Arai, 1992. Rapid and continuous hydrothermal crystallization of metal-oxide particles in supercritical water. J. Am. Ceram. Soc. 75, 1019–1022.

Adschiri T., Y. Hakuta, K. Sue & K. Arai, 2001. Hydrothermal synthesis of metal oxide nanoparticles at supercritical conditions. J. Nanopart. Res. 3, 227–235.

Bonnemann H., G. Braun, W. Brijoux, R. Brinkmann, A.S. Tilling, K. Seevogel & K. Siepen, 1996. Nanoscale colloidal metals and alloys stabilized by solvents and surfactants – Preparation and use as catalyst precursors. J. Organomet. Chem. 520, 143–162.

Horn D. & J. Rieger, 2001. Organic nanoparticles in the aqueous phase – theory, experiment, and use. Angew. Chem. Int. Ed. 40, 4331–4361.

Li L.M., E. Beniash, E.R. Zubarev, W. Xiang, B.M. Rabatic, G. Zhang & S.I. Stupp, 2003. Assembling a lasing hybrid material with supramolecular polymers and nanocrystals. Nat. Mater. 2, 689–694.

Mousavand T., S. Takami, M. Umetsu, S. Ohara & T. Adschiri, 2006a. Supercritical hydrothermal synthesis of organic–inorganic hybrid nanoparticles. J. Mater. Sci. 41, 1445–1448.

Mousavand T., S. Ohara, M. Umetsu, J. Zhang, S. Takami, T. Naka & T. Adschiri, 2006b. Hydrothermal synthesis and in situ surface modification of boehmite nanoparticles in supercritical water. J. Supercritical Fluids. (accepted).

Sanchez C., G.J. De, F. Ribot, T. Lalot, C.R. Mayer & V. Cabuil, 2001. Designed hybrid organic–inorganic nanocomposites from functional nanobuilding blocks. Chem. Mater. 13, 3061–3083.

Singhal A., G. Skandan, A. Wang, N. Glumac, B.H. Kear & R.D. Hunt, 1999. On nanoparticle aggregation during vapor phase synthesis. Nanostruct. Mater. 11, 545–552.

ELSEVIER

Journal of Biomechanics 40 (2007) 2752–2757

JOURNAL OF BIOMECHANICS

www.elsevier.com/locate/jbiomech
www.JBiomech.com

In vitro confocal micro-PIV measurements of blood flow in a square microchannel: The effect of the haematocrit on instantaneous velocity profiles

Rui Lima[a,b,*], Shigeo Wada[c], Motohiro Takeda[a,d], Ken-ichi Tsubota[a], Takami Yamaguchi[a]

[a]*Department of Bioengineering and Robotics, Graduate School of Engineering, Tohoku University, 6-6-01 Aoba, 980-8579 Sendai, Japan*
[b]*Department of Mechanical Technology, ESTiG, Bragança Polytechnic Institute, Campus Sta. Apolónia, 5301-857 Bragança, Portugal*
[c]*Department of Mechanical Science and Bioengineering, Graduate School of Engineering Science, Osaka University, Toyonaka, 560-8531 Osaka, Japan*
[d]*Division of Surgical Oncology, Graduate School of Medicine, Tohoku University, 2-1 Seiryo-machi, Aoba-ku, 980-8575 Sendai, Japan*

Accepted 16 January 2007

Abstract

A confocal microparticle image velocimetry (micro-PIV) system was used to obtain detailed information on the velocity profiles for the flow of pure water (PW) and in vitro blood (haematocrit up to 17%) in a 100-μm-square microchannel. All the measurements were made in the middle plane of the microchannel at a constant flow rate and low Reynolds number ($Re = 0.025$). The averaged ensemble velocity profiles were found to be markedly parabolic for all the working fluids studied. When comparing the instantaneous velocity profiles of the three fluids, our results indicated that the profile shape depended on the haematocrit. Our confocal micro-PIV measurements demonstrate that the root mean square (RMS) values increase with the haematocrit implying that it is important to consider the information provided by the instantaneous velocity fields, even at low *Re*. The present study also examines the potential effect of the RBCs on the accuracy of the instantaneous velocity measurements.
© 2007 Elsevier Ltd. All rights reserved.

Keywords: Microcirculation; Confocal micro-PIV; Instantaneous velocity profiles; Haematocrit; Red blood cells

1. Introduction

The velocity profiles of blood flow in vivo and in vitro have been measured using several techniques, including double-slit photometry (Gaehtgens et al., 1970; Baker and Wayland, 1974), video microscopy and image analysis (Bugliarello and Hayden, 1963; Tangelder et al., 1986; Parthasarathi et al., 1999), laser-Doppler anemometry (Einav et al., 1975; Born et al., 1978; Cochrane et al., 1981; Uijttewaal et al., 1994, Golster et al., 1999), and particle-measuring methods (Sugii et al., 2002, 2005; Nakano et al., 2003, 2005; Jeong et al., 2007). Nevertheless, no general consensus yet exists concerning the actual velocity profile in microvessels. While some studies have reported parabolic profiles (Baker and Wayland, 1974; Golster et al., 1999; Sugii et al., 2005), others have suggested blunt profiles (Bugliarello and Hayden, 1963; Tangelder et al., 1986; Nakano et al., 2003); still others have reported blunt profiles at extremely low velocities and diameters and parabolic profiles at diameters exceeding 100 μm (Gaehtgens et al., 1970; Cochrane et al., 1981). Thus, further research is needed on the influence of flow parameters on the blood flow velocity profiles in microvessels.

Due to its outstanding spatial filtering technique and multiple point light illumination system, confocal microparticle image velocimetry (micro-PIV) (Tanaani et al., 2002; Park et al., 2004; Kinoshita et al., 2005; Park and Kihm, 2006; Lima et al., 2006a) has become accepted as a reliable method for measuring velocity profiles with high spatial resolution. Very recently, we demonstrated the ability of confocal micro-PIV to measure both homogeneous and nonhomogeneous fluids (Lima et al., 2006a).

*Corresponding author. Tel.: +81 22 7956958; fax: +81 22 7956959.
E-mail address: rui@pfsl.mech.tohoku.ac.jp (R. Lima).

0021-9290/$ - see front matter © 2007 Elsevier Ltd. All rights reserved.
doi:10.1016/j.jbiomech.2007.01.012

The present study compared the instantaneous and ensemble velocities profiles of pure water and blood flow in vitro. The velocity profiles of both pure water and in vitro blood with two different haematocrits (9 and 17% Hct) were acquired in the centre plane of a 100-μm square microchannel.

2. Materials and methods

2.1. Working fluids and microchannel

This study examined three working fluids: pure water (PW) and physiological saline (PS) containing 9% (9 Hct) or 17% (17 Hct) human red blood cells (RBCs). All the fluids were seeded with 0.15% (by volume) 1-μm-diameter red fluorescent solid polymer microspheres (R0100; Duke Scientific, Palo Alto, CA, USA). The blood used was collected from a healthy adult volunteer, and ethylenediaminetetraacetic acid (EDTA) was added to prevent coagulation. The RBCs were separated from the bulk blood by centrifugation (1500 rpm for 20 min) and the plasma and buffy coat were removed by aspiration. The washing and centrifuging with PS was repeated twice. The remaining RBCs were then resuspended in PS to make up the required RBC concentration by volume. The haematocrit of the two RBC suspensions used in this study was about 9% (9 Hct) and 17% (17 Hct), respectively. All the blood samples were stored hermetically at 4 °C until the experiment was performed at room temperature (25–27 °C).

In this study, we used a 100-μm-square borosilicate glass microchannel fabricated by Vitrocom (Mountain Lakes, NJ, USA), which was mounted on a glass slide immersed in glycerol that had the same refractive index. A square microchannel was selected to minimise possible refraction of the laser beam at the walls of the microchannel. Using a glass tube, the refraction arising from the curved walls would be more pronounced and might degrade the measured velocity fields.

2.2. Experimental setup

The confocal micro-PIV system we used consisted of an inverted microscope (IX71; Olympus, Tokyo, Japan) combined with a confocal scanning unit (CSU22; Yokogawa Corporation, Tokyo, Japan) and a diode-pumped solid-state (DPSS) continuous wave (CW) laser (Laser Quantum, Stockport, UK) with an excitation wavelength of 532 nm. A high-speed camera (Phantom v7.1; Vision Research, Wayne, NJ, USA) was connected to the outlet port of the CSU22. The microchannel was placed on the stage of an inverted microscope and the flow rate (Q) of the working fluids was kept constant at 0.15 μl/min using a syringe pump (KD Scientific, Holliston, MA, USA), corresponding to a Reynolds number (Re) of 0.025.

The laser beam was illuminated from below the microscope stage through a 20 × objective dry lens with a numerical aperture (NA) equal to 0.75. Satisfactory illumination was achieved by seeding 1-μm-diameter fluorescent particles that absorb green light (absorbance peak 542 nm) and emit red light (emission peak 612 nm). The light emitted from the fluorescent flowing particles passes through a colour filter into the CSU22 scanning unit, where it is reflected onto a high-speed camera using a dichromatic mirror to record the PIV images.

In order to obtain adequate quality images for processing with the PIV software (PivView; PivTec GmbH, Göttingen, Germany), we captured images with a resolution of 640 × 480 pixels and 12-bit greyscale, at a rate of 200 frames/s, with an exposure time of 4995 μs, and a time interval (Δt) of 5 and 10 ms between two images. All the PIV measurements were performed for a period of approximately 0.5 s in order to obtain both instantaneous and ensemble averaged velocities. After recording the images, they were digitised and transferred to a computer for evaluation using Phantom camera control software (PH607). The PIV images of the flowing particles were processed and the flow velocity was determined using PivView version 2.3 (Raffel et al., 1998). The images were evaluated using a cross-correlation method in which the time between two images was set to 5 and 10 ms for all working fluids. Using a multiple-pass interrogation algorithm with a 24 × 16 pixel interrogation window (50% overlap), which corresponds to a spatial resolution of 28.24 × 18.83 μm, it was possible to obtain the corresponding instantaneous and ensemble velocity fields. A full description and evaluation of the confocal micro-PIV system used in this study can be found in Lima et al. (2006a).

3. Results and discussion

3.1. Ensemble velocity profiles

Most previous studies have determined the velocity profiles of flowing blood by measuring the time-averaged velocity field. Fig. 1(a) and (b) shows the averaged velocity of 100 ($\Delta t = 5$ ms) and 50 ($\Delta t = 10$ ms) ensemble PIV images, respectively. These images were recorded at the same time period of approximately 0.5 s. Fig. 1 also compares the PIV measurements with an analytical solution for steady flow through a long, straight, rigid square microchannel (see Lima et al., 2006a for more details).

Comparing the ensemble velocity profiles of all fluids (see Fig. 1), we observed small deviations (<5%) for both $\Delta t = 5$ and 10 ms, especially in the central region of the velocity profile. Using the t-test analysis we found no significant difference between the working fluids and the analytical solution at 98% confidence interval. Hence, these results imply that the ensemble-averaged velocity profiles of in vitro blood with haematocrits up to 17% flowing within a 100-μm square microchannel do not change significantly from a parabolic shape. These results agree with Baker and Wayland (1974) and Sugii et al. (2005). Furthermore, from the ensemble-averaged velocity profiles for both $\Delta t = 5$ and 10 ms the average deviation was estimated to be 2% for PW and 17% Hct and 5% for 9% Hct. On comparing the results from both Δt we found no significant difference between $\Delta t = 5$ and 10 ms at 98% confidence interval. These results suggest that for both cases it is possible to obtain reliable ensemble-averaged velocity profiles for all the working fluids used in this study.

3.2. Instantaneous velocity profiles and root mean square (RMS)

A remarkable advantage of the PIV measuring technique over conventional methods, such as double-slit photometry or laser–Doppler anemometry, is its ability to obtain detailed information on the fluid flow behaviour from the evaluation of the instantaneous velocity fields. Although these velocity fields are extremely important for flows with high Re in which turbulent flow fields are likely to occur (Meinhart et al., 2000a; Bates et al., 2001; Heise et al., 2004), we believe that instantaneous velocities are also crucial for evaluating several phenomena in steady flows, especially for complex fluids containing suspended blood cells in plasma. In this way, Figs. 2–4 show the first time series of the instantaneous velocity profiles of pure water

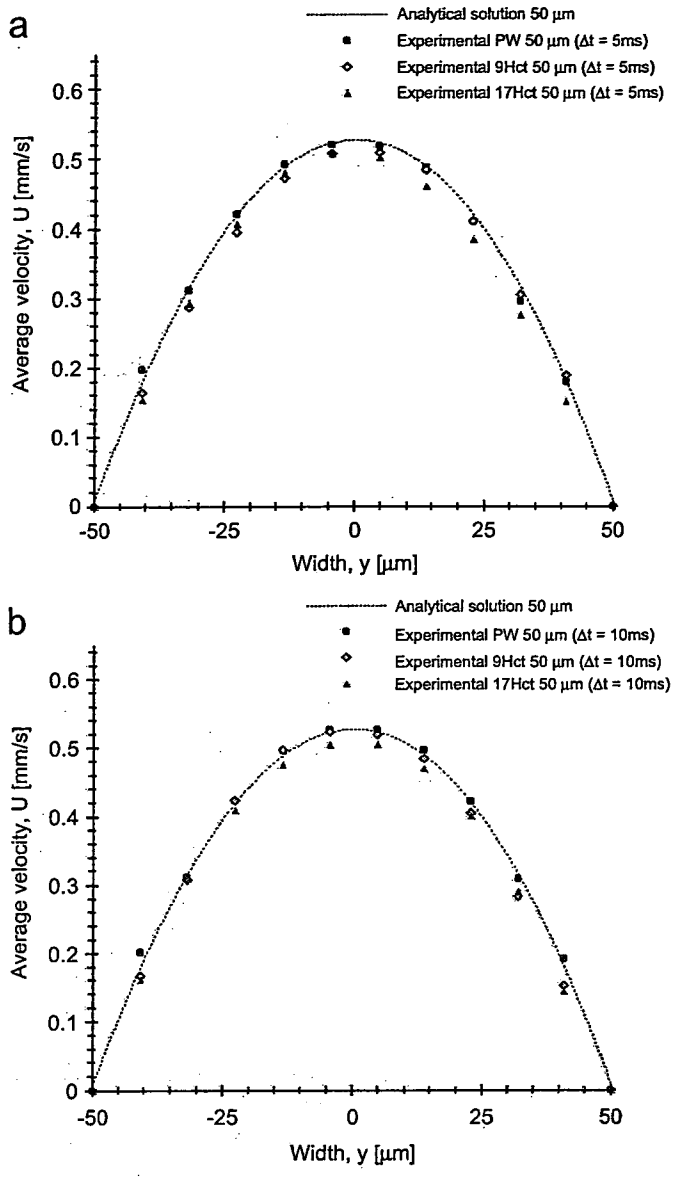

Fig. 1. Averaged ensemble velocity profiles for six different series of confocal micro-PIV measurements in the central plane (50 μm) of: (a) pure water (PW) and in vitro blood with haematocrit 9% (9 Hct) and 17% (17 Hct) for $\Delta t = 5$ ms; (b) pure water (PW) and in vitro blood (9 and 17 Hct) for $\Delta t = 10$ ms.

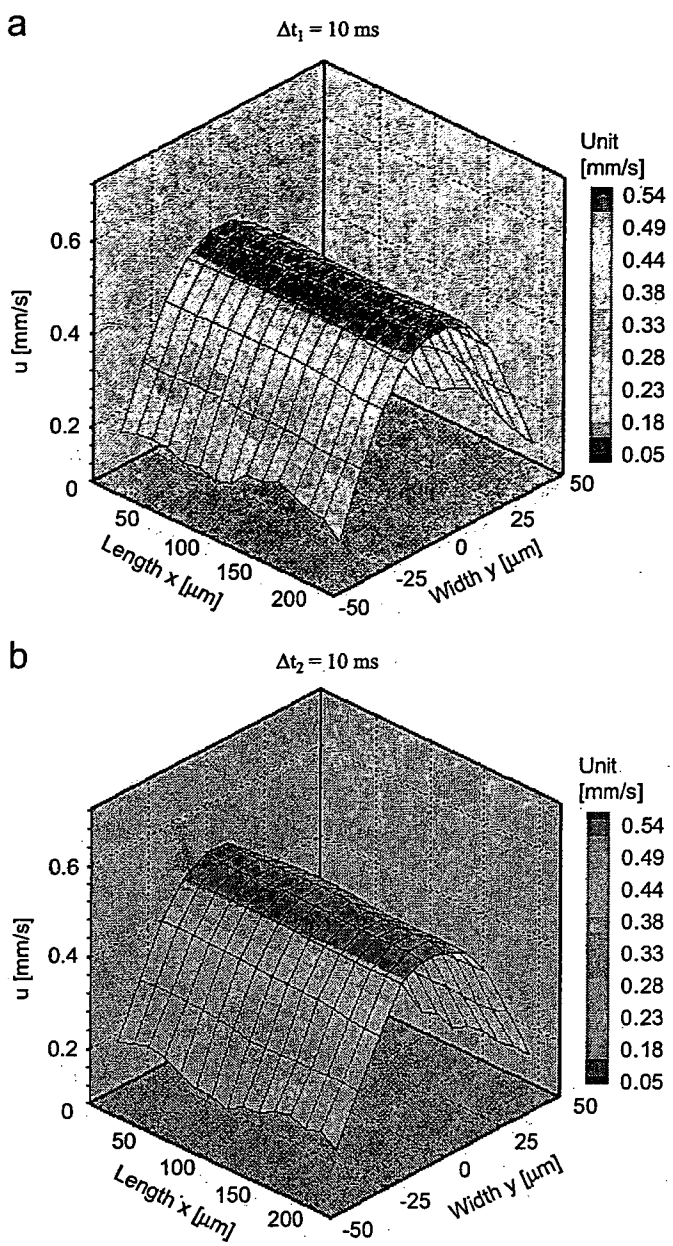

Fig. 2. Two examples showing series of instantaneous velocity profiles of pure water (PW) in the central plane (50 μm) of the microchannel for $\Delta t = 10$ ms. Note that, x, y represent, respectively, measured length and full-width of the microchannel whereas u represents the axial velocity of the working fluid along the central plane of the microchannel.

and in vitro blood with two different haematocrits at Re 0.025 for $\Delta t = 10$ ms.

In the conventional micro-PIV, most of the noise in the instantaneous velocity measurements is mainly due to the out-of-focus particle images, Brownian motion and low particle image density (Santiago et al., 1998; Nguyen and Wereley, 2002). The standard method to improve the accuracy of the conventional micro-PIV measurements is by ensembling series of instantaneous velocities. However, very recently it was shown that confocal micro-PIV, due to its optical sectioning effect provided by the spinning disk, can improve significantly the background noise even when using high particle concentration, i.e., 0.1% by volume (Park et al., 2004; Park and Kihm, 2006; Lima et al., 2006a). Furthermore, by using trace particles with 1 μm diameter it is possible to minimise some possible Brownian motion effect (Santiago et al., 1998). As a result, we believe that confocal micro-PIV can provide reliable instantaneous velocity fields, especially for homogenous fluids and in vitro blood with low haematocrit (Hct$\leqslant$9%) (see Appendix A).

On comparing the instantaneous velocity fields in the middle plane of pure water and in vitro blood (see Figs. 2–4), it is possible to observe that the instantaneous velocities from pure water have a nearly constant parabolic profile, whereas the instantaneous velocities from both in

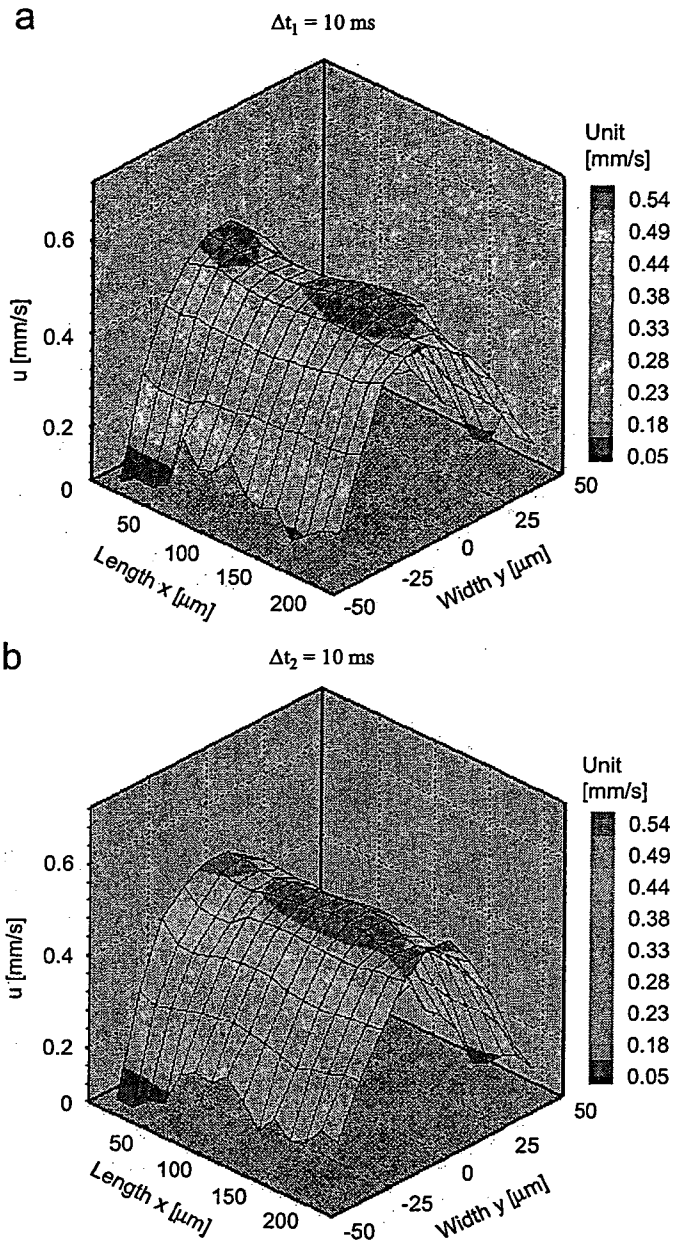

Fig. 3. Two examples showing series of instantaneous velocity profiles of in vitro blood with a 9% (9 Hct) haematocrit in the central plane of the microchannel for $\Delta t = 10$ ms.

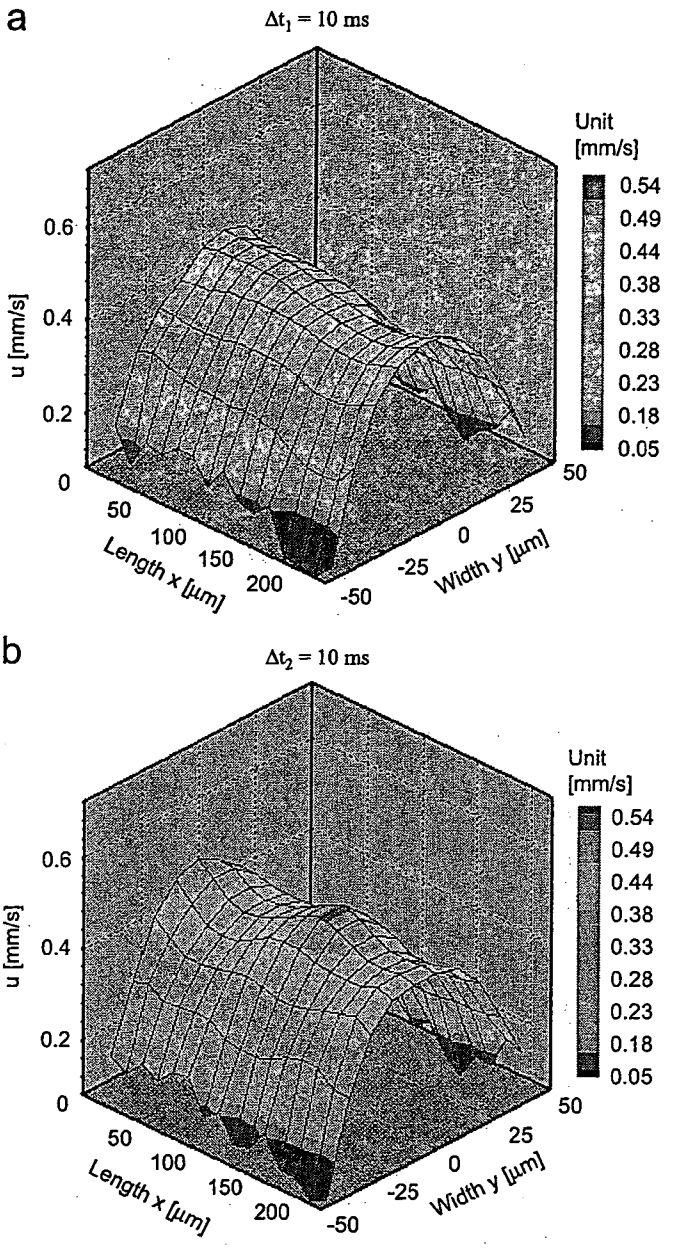

Fig. 4. Two examples showing series of instantaneous velocity profiles of in vitro blood with a 17% (17 Hct) haematocrit in the central plane of the microchannel for $\Delta t = 10$ ms.

vitro blood show some irregularities on the velocity profiles. However, these instantaneous velocity profiles are only qualitative observations which needed to be quantified in order to understand the possible causes of the fluctuations encountered on the in vitro blood instantaneous velocity profiles (see Figs. 3 and 4).

In an attempt to elucidate the possible causes of these findings we have calculated the RMS which can be determined from the ensemble averaging of the instantaneous velocity measurements. To calculate the RMS we first need to determine the standard deviation of both u and v components of the velocity at each grid point for a series of N frames using the following equations:

mean velocity components:

$$\bar{u} = \frac{1}{N}\sum_{i=1}^{N} u_i, \tag{1}$$

$$\bar{v} = \frac{1}{N}\sum_{i=1}^{N} v_i, \tag{2}$$

standard deviation of u and v components:

$$\sigma_u = \sqrt{\sum_{i=1}^{N}(u_i - \bar{u})^2/N - 1}, \tag{3}$$

$$\sigma_v = \sqrt{\sum_{i=1}^{N}(v_i - \bar{v})^2/N - 1}. \quad (4)$$

After calculating both σ_u and σ_v, RMS can be estimated by

$$\mathrm{RMS} = \sqrt{\sigma_u^2 + \sigma_v^2}. \quad (5)$$

In Fig. 5 the averaged RMS values for the three working fluids at two different Δt are plotted as a function of the microchannel width.

On comparing the RMS values with different Δt it is possible to observe that by increasing the time interval between two images the RMS decreases about 50% for PW and 9% Hct and 25% for 17% Hct. Therefore, using $\Delta t = 10$ ms the accuracy of the instantaneous velocity measurements are improved implying that the correspondent RMS values may represent a more reliable qualitative information about the time-dependent behaviour of the flow. Moreover, on comparing the RMS values from all the working fluids we have found that there is a significant difference between PW, 9 and 17% Hct at 90% confidence interval, except for some values near the wall (see Fig. 5). Despite the inclusion of some bias errors in the RMS values (see Appendix A), these results show clearly that the RMS increases with the haematocrit. We believe that the RMS values are strongly related to the fluctuations encountered in the instantaneous velocity profiles shown in Figs. 3 and 4. The reasons for these small fluctuations are still not completely clear, however, from the visualisation of the RBCs motion through the microchannel, both rotational and tumbling motion and also the interaction between the neighbouring RBCs seem to be important factors to take into account. An ongoing study to clarify the effect of the RBCs on the plasma flow is currently under way.

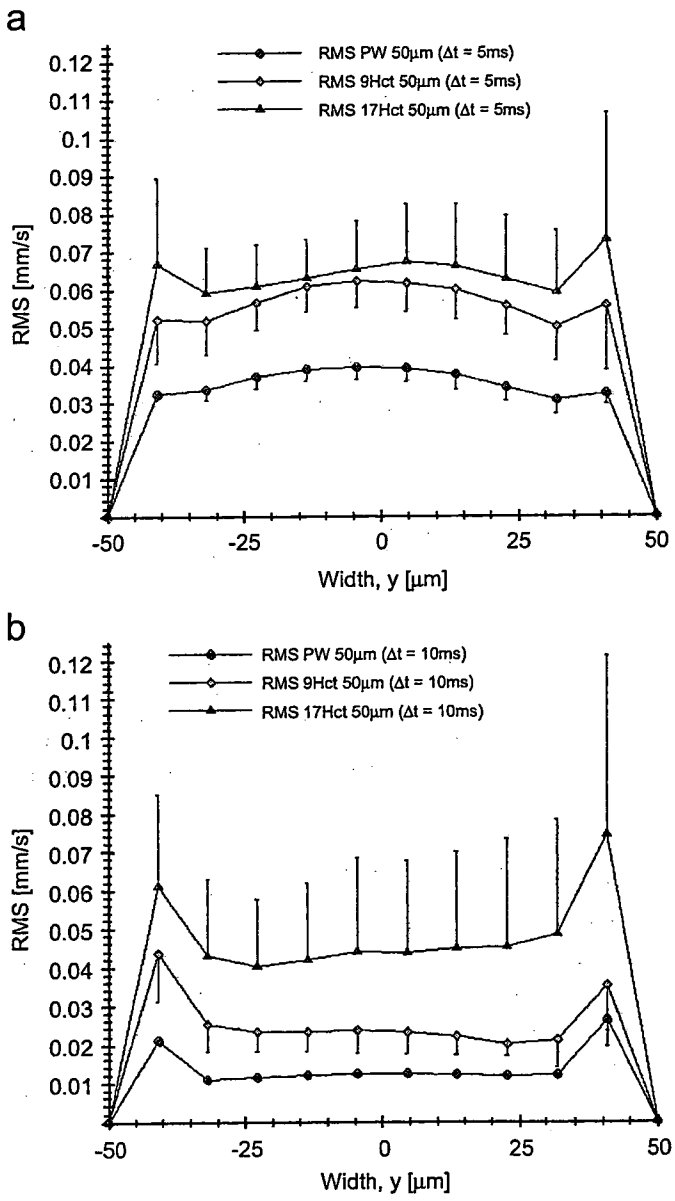

Fig. 5. Comparison of the RMS values for pure water (PW) and in vitro blood with haematocrits of 9% (9 Hct) and 17% (17 Hct) with (a) $\Delta t = 5$ ms, (b) $\Delta t = 10$ ms.

It should be noted that for haematocrits of about 17% we have observed some small random "plasma pockets" without particles in the PIV images which have created velocity vectors with small magnitudes mainly due to the light scattered and absorbed from the high concentration of RBCs within the plasma flow. Therefore, the RMS values for Hct = 17% contains quantitative information about not only the effect of the RBCs on the plasma flow but also some bias errors (see Appendix A). One way to overcome this limitation is by increasing the particles concentration within the plasma or by using a rectangular microchannel with low aspect ratio which creates an uniform distribution of RBCs (Lima et al., 2006b).

4. Conclusions

In this study, we determined both ensemble and instantaneous velocity profiles for in vitro blood (haematocrit up to 17%) flowing through a 100-μm-square microchannel. Although the ensemble velocity profiles were markedly parabolic, some fluctuations in the instantaneous velocity profiles were found to be closely related to the increase in the haematocrit. The present study shows clearly that the RMS values increase with the haematocrit implying that the presence of RBCs within the plasma flow strongly influences the measurements of the instantaneous velocity fields. The possible reasons for the RMS increase are the motion and interaction of RBCs and the light scattered and absorbed from the RBCs. This latter cause seems to be more predominant at Hct = 17%. As a result, for 17% Hct improvements on the signal-to-noise ratio are required to further enhance the measurement performance of the instantaneous velocities.

Acknowledgements

This study was supported in part by the following grants: International Doctoral Program in Engineering from the Ministry of Education, Culture, Sports, Science and Technology of Japan (MEXT), "Revolutionary Simulation Software (RSS21)" next-generation IT program of MEXT; Grants-in-Aid for Scientific Research from MEXT and JSPS Scientific Research in Priority Areas (768) "Biomechanics at Micro- and Nanoscale Levels," Scientific Research (A) no. 16200031 "Mechanism of the formation, destruction, and movement of thrombi responsible for ischemia of vital organs". The authors would like to thank Dr. Takuji Ishikawa for his valuable suggestions and discussion.

Appendix A. Supplementary data

Supplementary data associated with this article can be found, in the online version; at doi:10.1016/j.jbiomech.2007.01.012.

References

Bates, C., O'Doherty, D., Williams, D., 2001. Flow instabilities in a graft anstomosis: a study of instantaneous velocity fields. Proceedings of the Institution of Mechanical Engineers Part H 215, 579–587.

Baker, M., Wayland, H., 1974. On-line volume flow rate and velocity profile measurement for blood in microvessels. Microvascular Research 7, 131–143.

Born, G., Melling, A., Whitelaw, J., 1978. Laser Doppler microscope for blood velocity measurement. Biorheology 15, 163–172.

Bugliarello, G., Hayden, J., 1963. Detailed characteristics of the flow of blood *in vitro*. Transactions of The Society Rheology 7, 209–230.

Cochrane, T., Earnshaw, J., Love, A., 1981. Laser Doppler measurement of blood velocity in microvessels. Medical and Biological Engineering and Computing 19, 589–596.

Einav, S., Berman, R., Fuhro, P., DiGiovanni, P., Fine, S., Fridman, J., 1975. Measurement of velocity profiles of red blood cells in the microcirculation by laser Doppler anemometry (LDA). Biorheology 12, 207–210.

Gaehtgens, P., Meiselman, H., Wayland, H., 1970. Velocity profiles of human blood at normal and reduced hematocrit in glass tubes up to 130 μ diameter. Microvascular Research 2, 13–23.

Golster, H., Linden, M., Bertuglia, S., Colantuoni, A., Nilsson, G., Sjoberg, F., 1999. Red blood cell velocity and volumetric flow assessment by enhanced high-resolution laser Doppler imaging in separate vessels of hamster cheek pouch microcirculation. Microvascular research 58, 62–73.

Heise, M., Schmidt, S., Kruger, U., Ruckert, R., Rosler, S., Neuhaus, P., Settmacher, U., 2004. Flow pattern and shear stress distribution of distal end-to-side anastomoses. A comparison of instantaneous velocity fields obtained by particle image velocimetry. Journal of Biomechanics 37, 1043–1051.

Jeong, J.H., Sugii, Y., Minamiyama, M., Takeuchi, H., Okamoto, K., 2007. Interaction between liposomes and RBC in microvessels in vivo. Microvascular Research 73, 39–47.

Kinoshita, H., Oshima, M., Kaneda, S., Fujii, T., 2005. Confocal micro-PIV measurement of internal flow in a moving droplet. In: Proceedings of the Ninth International Conference on Miniaturized Systems for Chemistry and Life Sciences. Boston, MA, USA.

Lima, R., Wada, S., Tsubota, K., Yamaguchi, T., 2006a. Confocal micro-PIV measurements of three dimensional profiles of cell suspension flow in a square microchannel. Measurement Science and Technology 17, 797–808.

Lima, R., Wada, S.,Tanaka, S., Takeda, M., Tsubota, K., Ishikawa T., Yamaguchi, T., 2006b. Velocity measurements of blood flow in a rectangular PDMS microchannel assessed by confocal micro-PIV system. In: Proceedings of the World Congress on Medical Physics and Biomedical Engineering. Seoul, pp. 278–281.

Meinhart, C., Wereley, S., Santiago, J., 2000. A PIV algorithm for estimating time-averaged velocity fields. Journal of Fluids Engineering 122, 285–289.

Nakano, A., Sugii, Y., Minamiyama, M., Niimi, H., 2003. Measurement of red cell velocity in microvessels using particle image velocimetry (PIV). Clinical Hemorheology and Microcirculation 29, 445–455.

Nakano, A., Sugii, Y., Minamiyama, M., Seki, J., Niimi, H., 2005. Velocity profiles of pulsatile blood flow in arterioles with bifurcation and confluence in rat mesnetery measured by particle image velocimetry. JSME International Journal C 48 (4), 444–452.

Nguyen, N., Wereley, S., 2002. Fundamentals and Applications of Microfluidics. Artech House Inc., Norwood, MA, USA.

Park, J., Choi, C., Kihm, K., 2004. Optically sliced micro-PIV using confocal laser scanning microscopy (CLSM). Experiments in Fluids 37, 105–119.

Park, J., Kihm, K., 2006. Use of confocal laser scanning microscopy (CLSM) for depthwise resolved microscale-particle image velocimetry (μ-PIV). Optics and Lasers in Engineering 44, 208–223.

Parthasarathi, A., Japee, S., Pittman, R., 1999. Determination of red blood cell velocity by video shuttering and image analysis. Annals of Biomedical Engineering 27, 313–325.

Raffel, M., Willert, C., Kompenhans, J., 1998. Particle Image Velocimetry: A Practical Guide. Springer, Germany.

Santiago, J., Wereley, S., Meinhart, C., Beebe, D., Adrian, R., 1998. A particle image velocimetry system for microfluidics. Experiments in Fluids 25, 316–319.

Sugii, Y., Nishio, S., Okamoto, K., 2002. *In vivo* PIV measurement of red blood cell velocity field in microvessels considering mesentery motion. Physiological Measurement 23, 403–416.

Sugii, Y., Okuda, R., Okamoto, K., Madarame, H., 2005. Velocity measurement of both red blood cells and plasma of *in vitro* blood flow using high-speed micro PIV technique. Measurement Science and Technology 16, 1126–1130.

Tangelder, G., Slaaf, D., Muijtjens, M., Arts, T., Egbrink, M., Reneman, R., 1986. Velocity profiles of blood platelets and red blood cells flowing in arteriols of rabbit mesentery. Circulation Research 59, 505–514.

Tanaani, T., Otsuki, S., Tomosada, N., Kosugi, Y., Shimizu, M., Ishida, H., 2002. High-speed 1-frame/ms scanning confocal microscope with a microlens and Nipkow disks. Applied Optics 41 (22), 4704–4708.

Uijttewaal, W., Nijhof, E., Heethaar, R., 1994. Lateral migration of blood cells and microspheres in two-dimensional Poiseuille flow: a laser Doppler study. Journal of Biomechanics 27, 35–42.

Available online at www.sciencedirect.com
ScienceDirect
ELSEVIER
Colloids and Surfaces A: Physicochem. Eng. Aspects xxx (2007) xxx–xxx
COLLOIDS AND SURFACES A
www.elsevier.com/locate/colsurfa

Preparation of multilayered silica–Gd–silica core-shell particles and their magnetic resonance images

Yoshio Kobayashi [a], Junichi Imai [b], Daisuke Nagao [b], Motohiro Takeda [c], Noriaki Ohuchi [c], Atsuo Kasuya [d], Mikio Konno [b,*]

[a] *Department of Biomolecular Functional Engineering, College of Engineering, Ibaraki University, 4-12-1 Naka-narusawa-cho, Hitachi, Ibaraki 316-8511, Japan*
[b] *Department of Chemical Engineering, Graduate School of Engineering, Tohoku University, 6-6-07 Aoba, Aramaki-aza, Aoba-ku, Sendai 980-8579, Japan*
[c] *Division of Surgical Oncology, Graduate School of Medicine, Tohoku University, Seiryo-machi, Aoba-ku, Sendai 980-8574, Japan*
[d] *Center for Interdisciplinary Research, Tohoku University, Aoba, Aramaki-aza, Aoba-ku, Sendai 980-8578, Japan*

Received 30 March 2007; received in revised form 10 May 2007; accepted 15 May 2007

Abstract

A preparation method for multilayered silica–Gd–silica core-shell particles is proposed. Silica particles with an average size of 30.9 nm were prepared by the Stöber method. Silica–Gd core-shell particles with a size of 57.4 nm were synthesized by a homogeneous precipitation method at 80 °C in water/propanol solution with 27.7 M H_2O, 0.001 M $Gd(NO_3)_3$, 0.5 M urea and 1 g/l polyvinylpyrrolidone in the presence of 0.001 vol.% suspension of the silica particles. Succeeding silica-coating of the silica–Gd core-shell particles was performed with 0.0133 M TEOS and 0.002 M NaOH in the presence of a suspension of silica–Gd core-shell particles. Consequently, multilayered silica–Gd–silica core-shell particles with an average size of 71.2 nm could be obtained. These particles exhibited clear enhancement in magnetic resonance images. These nanoparticles are expected to a novel magnetic resonance contrast agents.
© 2007 Published by Elsevier B.V.

Keywords: Multilayer; Core-shell; Particle; Silica; Gadolinium; Stöber method; Homogeneous precipitation method; MRI

1. Introduction

Various types of core-shell nanoparticles have been emerging, and they exhibited unique properties of magnetism, electronics and optics owing to their composite structure [1–12]. We have also produced various types of silica-coated nanoparticles with seeded polymerization techniques [13–21].

Imaging by X-ray and magnetic resonance (MR) has become very important diagnostic modalities in hospitals [22,23]. Iodine compounds [22] and gadolinium compounds [24] have been used as contrast agents for X-ray CT and magnetic resonance imaging, respectively. These existing compounds may provoke adverse events as allergic reactions in patients, so that they cannot be administered to such people [22,23]. Core-shell nanoparticles are good candidates for prevention of allergic reactions because the shell materials can keep the contrast agents from living systems. We have proposed a method for silica-coating of iodine compounds as AgI nanoparticles [17], and we obtained silica-coated AgI nanoparticles that could be used as contrast agents for X-ray CT [25].

The contrast agents should be stable as colloid or dispersed in biological systems, since aggregates cause restriction of blood flow and lymph flow. Since silica particles have good stability as colloids, three layered particles with silica core, layer of contrast agent and silica shell will be more stable than contrast agents without silica core. The silica core plays a role for stability of particles and the silica shell plays a role of insulation from outside the particle.

In this study, we employed gadolinium compounds for contrast agents and fabricated multilayered silica particles with the MR contrast agent. Silica–Gd core-shell particles are prepared with a homogeneous precipitation method, and the previously performed silica-coating method is extended to the silica–Gd

* Corresponding author. Tel.: +81 22 795 7239; fax: +81 22 795 7241.
E-mail address: konno@mickey.che.tohoku.ac.jp (M. Konno).

0927-7757/$ – see front matter © 2007 Published by Elsevier B.V.
doi:10.1016/j.colsurfa.2007.05.024

Please cite this article in press as: Y. Kobayashi et al., Preparation of multilayered silica–Gd–silica core-shell particles and their magnetic resonance images, Colloids Surf. A: Physicochem. Eng. Aspects (2007), doi:10.1016/j.colsurfa.2007.05.024

core-shell particles prepared. Verification of MR imaging is also performed for the multilayered particles.

2. Experimental

2.1. Materials

Tetraethylorthosilicate (TEOS) (96%), aqueous methyl amine (MA) (40% solution) and ethanol (99.5%) were used for preparation of silica cores and silica-coating as monomer, catalyst and solvent, respectively. Gadolinium nitrate hexahydrate ($Gd(NO_3)_3 \cdot 6H_2O$) (99.5%), urea (99.0%) and polyvinylpyrrolidone (PVP) (average molecular weight 36,000) were used as chemicals for Gd shell, a precipitation-inducer and a stabilizer of particles for Gd-coating, respectively. Polyvinylpyrrolidone was purchased from Nacalai Tesque Ltd. (Kyoto, Japan), and all the other chemicals were purchased from Wako Pure Chemicals Ltd (Osaka, Japan). All chemicals were used as received. Distilled and de-ionized water with an electrical resistance higher than 18 MΩ cm was used for all preparations.

2.2. Synthesis of particles

2.2.1. Silica particles

Colloidal suspensions of silica particles were prepared by a sol–gel method according to our previous paper [26]. Amine-catalytic reaction of TEOS in ethanol–water solution was carried out at initial concentrations of 0.2 M TEOS, 20 M H_2O and 0.018 M MA in a hermetically sealed flask with a magnetic stirrer. In each reaction, a solution of TEOS and ethanol was mixed with an aqueous MA solution stirring at 300 rpm and 35 °C for 24 h. Total volume of the reactant solution was about 400 ml. Colloidal suspensions of the silica particles were washed by repeating centrifugation, removal of supernatant, addition of the water and sonication over three times. Final volume of the suspension was adjusted to 20 ml with water. The silica concentration in the suspension was 0.96 vol.%, which was measured from the residue obtained after vaporization of the suspension. Fig. 1 shows TEM image of the silica particles. The silica particles were completely dispersed and had an average size of 31 ± 4 nm.

2.2.2. Silica–Gd particles

Gd-coating of the silica particles was performed by a homogeneous precipitation method in the presence of the silica particles. The Gd-coating in propanol–water solution was carried out at initial concentrations of 0.001 vol.% silica, 1 g/l PVP, 0.5 M urea and 0.001 M $Gd(NO_3)_3$ in a hermetically sealed flask reactor equipped with a mechanical stirrer. In each reaction, the silica suspension and the PVP aqueous solution were added to propanol–water solution under stirring at 300 rpm and a room temperature for 24 h. To the mixture successively added were aqueous urea solution, nitric acid (for adjusting pH to 5) and aqueous $Gd(NO_3)_3$. The mixture had a volume of about 200 ml and was stirred at 300 rpm and 80 °C for 3 h.

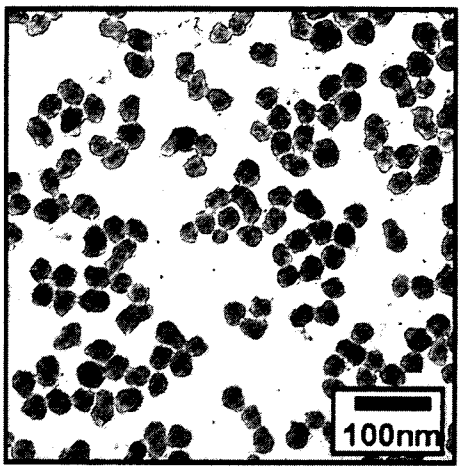

Fig. 1. TEM image of silica particles.

2.2.3. Silica–Gd–silica particles

Silica-coating of the silica–Gd core-shell particles was performed by a modified Stöber method. In each reaction, TEOS (0.59 ml) and 1.24 M aqueous NaOH solution (0.32 ml) were successively added to the suspension of silica–Gd particles (200 ml) in a hermetically sealed flask reactor equipped with a mechanical stirrer under stirring at 300 rpm and 35 °C for 24 h, which gave 0.0133 M TEOS and 0.002 M NaOH. Colloidal suspensions of silica–Gd–silica particles were washed by repeating centrifugation, removal of supernatant, addition of the water and sonication over three times.

2.3. Characterization

The particles were observed with a transmission electron microscope (TEM) (Zeiss LEO 912 OMEGA) operating at 100 kV and a scanning transmission electron microscope (STEM) (Hitachi High-Technologies HD-2000), equipped with an energy dispersive X-ray fluorescence spectrometer (EDX), operating at 200 kV. Samples for TEM and STEM were prepared by dropping and evaporating reactant mixture onto collodion-coated and uncoated copper grids, respectively. The study on the surface composition was performed using X-ray photoelectron spectroscopy (XPS). The XPS spectra were obtained by Phi 5700ci equipped with monochromatic Al Kα radiation (300 W, 14 kV, 1486.6 eV). Binding energies were calibrated relative to the C 1s peak (284.8 eV) from hydrocarbons adsorbed on the surface of the samples. To study on the composition underneath, the particle surface was etched with 2 kV Ar^+ sputtering with an etching rate of ca. 1.56 nm for one etching. ζ-Potential of particles was measured with an Ohtsuka ELS-8000 electrophretic light scattering spectrophotometer. Aqueous HCl solution or aqueous NaOH solution was added to the solution to vary pH of solution for ELS. For estimation of MR signal intensity, T1 weighted images of samples with 26 ms for the echo time and 800 ms for the repetition time were taken with a magnetic resonance imaging system (Vet-MR, ESAOTE SpA, Italy) at a static magnetic field of 0.4 T. The colloidal suspensions of particles that were washed by repeating centrifugation, removal of

Please cite this article in press as: Y. Kobayashi et al., Preparation of multilayered silica–Gd–silica core-shell particles and their magnetic resonance images, Colloids Surf. A: Physicochem. Eng. Aspects (2007), doi:10.1016/j.colsurfa.2007.05.024

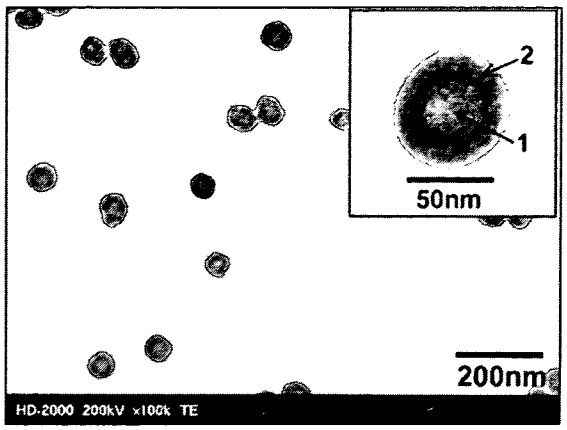

Fig. 2. STEM image of silica–Gd particles. Inset shows high-magnification image with points analyzed with EDX.

supernatant, addition of the water and sonication were used for the MR imaging.

3. Results and discussion

3.1. Silica–Gd core-shell particles

The silica–Gd particles exhibited no aggregation in the step of the Gd-coating of the silica particles, which indicated that colloidal stability of silica core particles prevented generation of aggregation. Fig. 2 shows STEM image of silica–Gd particles. The silica particles were coated with uniform shell. There was no uncoated silica particle or core-free particle. The average particle size was 57 ± 6 nm.

EDX spectra of the silica–Gd core-shell particles are shown in Fig. 3. The EDX analysis points are shown with arrows in the inset of Fig. 2. Assignments for main peaks were performed, as shown in Fig. 3. A carbon peak observed at 0.28 keV was

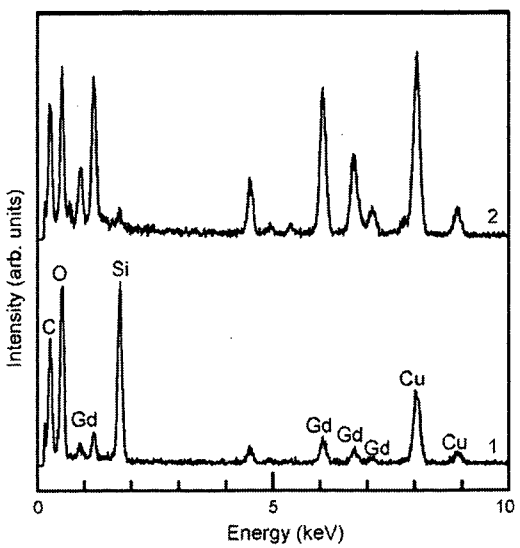

Fig. 3. EDX patterns of silica–Gd particles. Numbers 1 and 2 stand for the analysis points indicated with arrows in the inset of Fig. 2.

Table 1
EDX analysis results of silica–Gd particles

Point	Gd (at.%)	Si (at.%)
1	21.4	78.6
2	94.4	5.6

Analysis points 1 and 2 were indicated with arrows in the inset of Fig. 2.

due to contamination, and copper peaks at 8.04 and 8.90 keV were attributed to the copper grid. Peaks of SiK for 1.74 keV and GdL for 6.04 keV were used for estimation of chemical compositions. Table 1 shows results of the EDX analysis. The Gd/Si ratio of the core (point 1) and the shell (point 2) were 21.4 and 94.4 at.%, respectively. This result indicated that the shell was Gd-rich compared with the core. Accordingly, these results are the evidence that the Gd-coating of silica particles was successfully performed.

Fig. 4 shows the Gd $3d_{5/2}$ and Si 2p spectra of the silica–Gd core-shell particles. Gadolinium $3d_{5/2}$ peak intensity for the as-prepared silica–Gd particles (number of etching: 0) was small compared to those of the etched silica–Gd particles, since the surface of silica–Gd particles might be partially covered with carbon that was probably due to contamination. As the number of etching increased, a Si 2p peak appeared and was intensified. Fig. 5 shows atomic ratios for Gd + Si estimated from XPS peak area intensity in Fig. 4. Atomic ratios of Gd and Si for the as-prepared silica–Gd particles were 93 and 7%, respectively. This result indicated that the silica core was almost covered with Gd compounds. With an increase in the number of etching, the atomic ratio of Gd decreased to ca. 80%, and the Si ratio increased to ca. 20%. This result is also an evidence for the successful Gd-coating of silica particles.

3.2. Multilayered silica–Gd–silica core-shell particles

Fig. 6 shows STEM image of multilayered silica–Gd–silica core-shell particles. Only multilayered core-shell particles were observed, and there was no core-free silica or shell-free Gd–silica particles. The silica–Gd–silica particles had an average size of 71 ± 6 nm. It was confirmed by naked eye that no sedimentation took place for the silica–Gd–silica particle colloid in 24 h after preparation. In contrast, sedimentation was observed for the silica–Gd particle colloid in 24 h after preparation. This observation indicated that the silica shell contributed to the colloidal stability.

Fig. 7 shows the EDX spectra of the silica–Gd–silica particles. Table 2 shows results of the EDX analysis that were performed for points shown with arrows in the inset of Fig. 6.

Table 2
EDX analysis results of silica–Gd–silica particles

Point	Gd (at.%)	Si (at.%)
1	17.5	82.5
2	53.4	46.6
3	22.0	88.0

Analysis points 1–3 were indicated with arrows in the inset of Fig. 4.

Please cite this article in press as: Y. Kobayashi et al., Preparation of multilayered silica–Gd–silica core-shell particles and their magnetic resonance images, Colloids Surf. A: Physicochem. Eng. Aspects (2007), doi:10.1016/j.colsurfa.2007.05.024

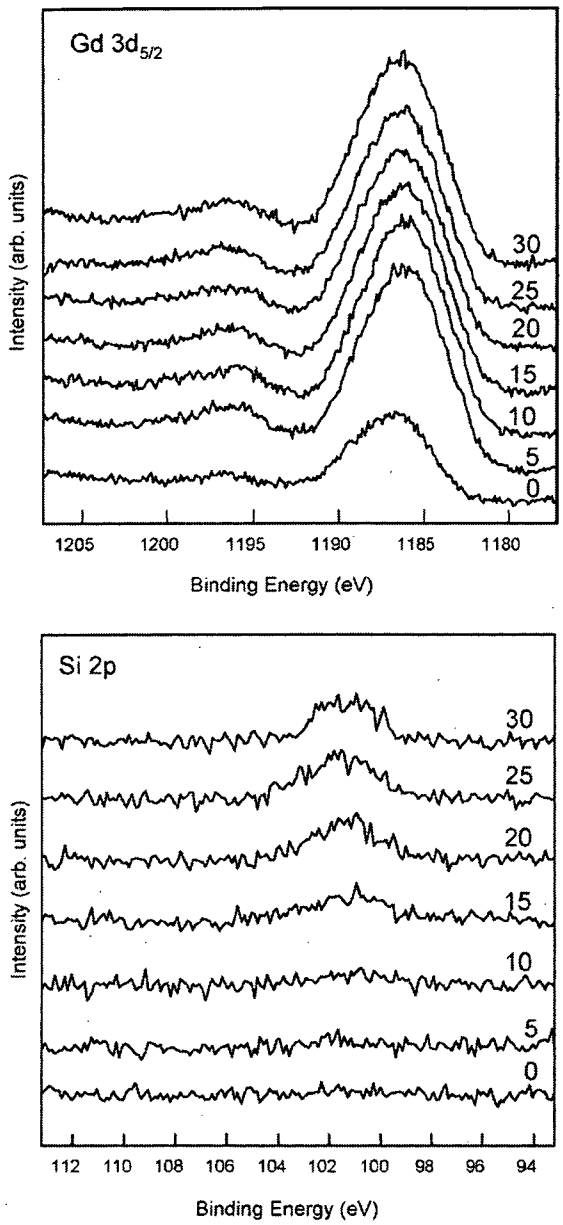

Fig. 4. XPS spectra of silica–Gd particles. Numbers 0–30 stand for number of Ar etching.

Similarly to the silica–Gd core-shell particles, the core (point 1) was Si-rich, and the inner shell on the silica core (point 2) was Gd-rich compared to the core. The Gd ratio in the outer shell on the silica–Gd core-shell particles (point 3) was 22.0 at.%, which was much lower than the inner shell. These results indicated that the silica–Gd core-shell particles were coated with silica.

Fig. 8 shows the Gd $3d_{5/2}$ and Si 2p spectra of the silica–Gd–silica particles. As the number of etching increased, an Si 2p peak intensity decreased, and in contrary, a Gd $3d_{5/2}$ peak intensity increased. Fig. 9 shows atomic ratios for Gd + Si estimated from XPS peak area intensity in Fig. 8. Atomic ratios of Gd and Si for the as-prepared silica–Gd–silica particles was almost 0 and 100%, respectively, which indicated that

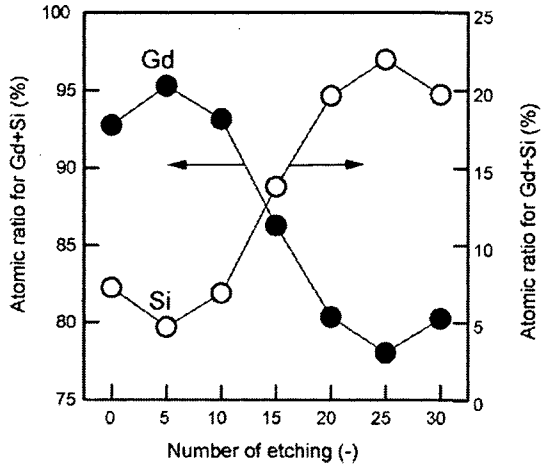

Fig. 5. Atomic ratios for Gd + Si of surface of silica–Gd particles as a function of number of Ar etching.

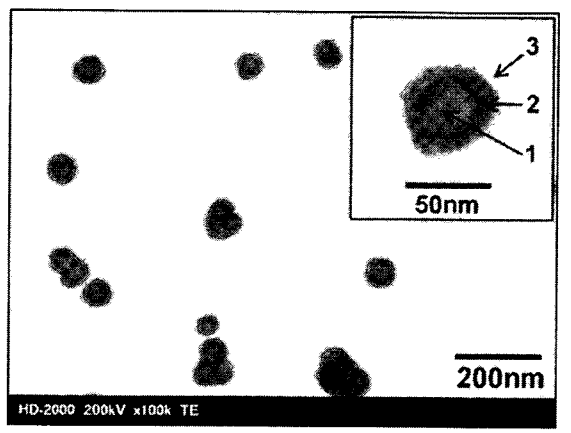

Fig. 6. STEM image of silica–Gd–silica particles. Inset shows high-magnification image with points analyzed with EDX.

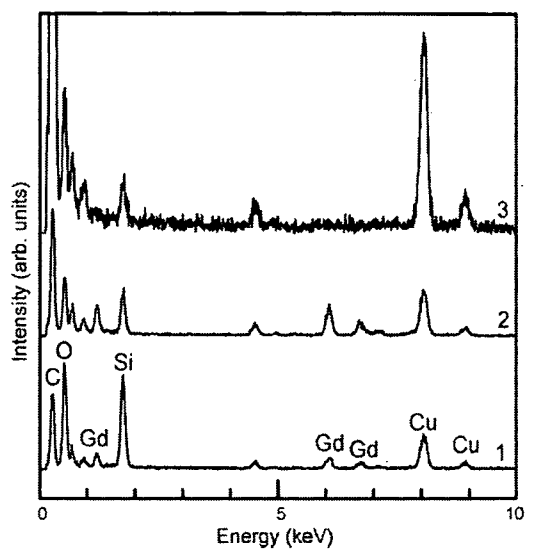

Fig. 7. EDX patterns of silica–Gd–silica particles. Numbers 1–3 stand for the analysis points indicated with arrows in the inset of Fig. 4.

Please cite this article in press as: Y. Kobayashi et al., Preparation of multilayered silica–Gd–silica core-shell particles and their magnetic resonance images, Colloids Surf. A: Physicochem. Eng. Aspects (2007), doi:10.1016/j.colsurfa.2007.05.024

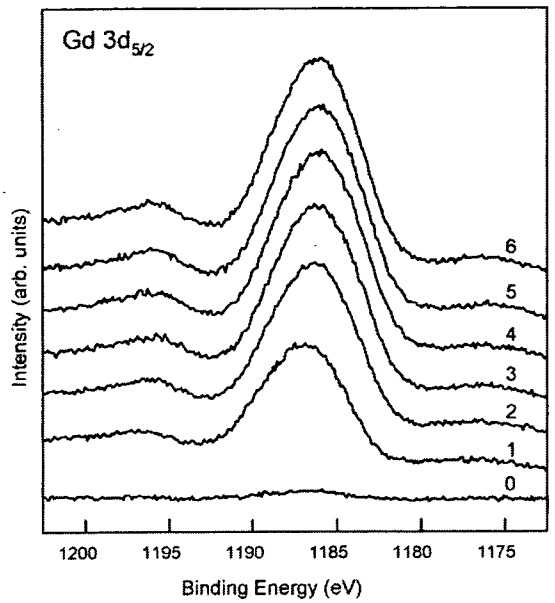

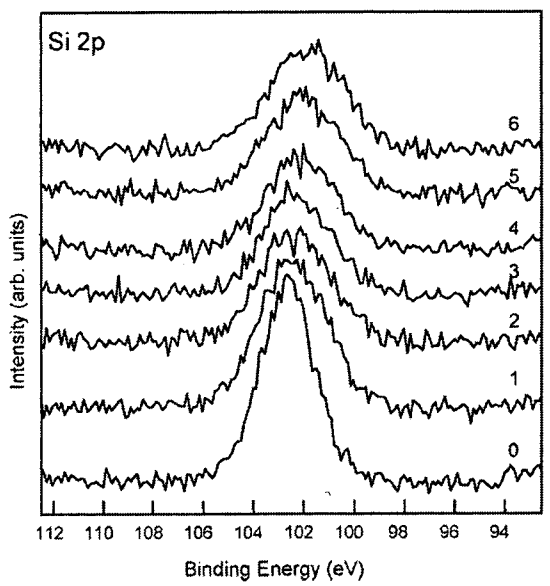

Fig. 8. XPS spectra of silica–Gd–silica particles. Numbers 0–6 stand for number of Ar etching.

the silica–Gd core was almost coated with silica. The atomic ratio of Gd increased to ca. 65%, and the Si ratio decreased to ca. 35% with the increase in the number of etching. This result indicated that the etching of outer silica shell revealed surface of silica–Gd particles, which also supported that the successful silica-coating of silica–Gd particles.

Fig. 10 shows the ζ-potentials of the silica, the silica–Gd and the silica–Gd–silica particles. Dispersion media of the as-prepared silica, silica–Gd and silica–Gd–silica particle colloids are considered to be water that contained no electrolytes, since the colloids were washed by repeating by centrifugation, removal of supernatant, addition of the water and sonication. The ζ-potentials of the as-prepared silica and the as-prepared silica–Gd particles were ca. −35 (pH 8.1) and ca. +13 mV (pH

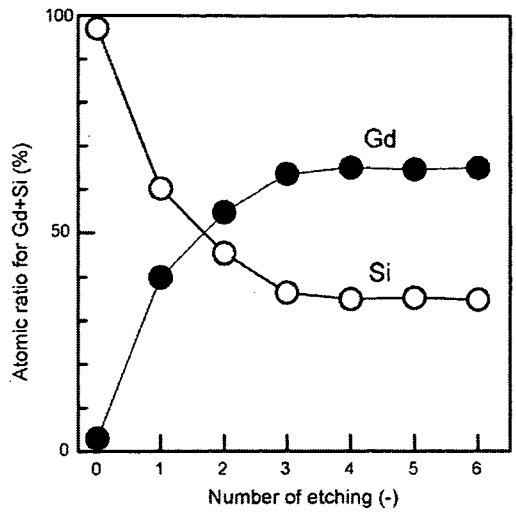

Fig. 9. Atomic ratios for Gd + Si of surface of silica–Gd–silica particles as a function of number of Ar etching.

8.0), respectively, which indicated that the silica particles were coated with Gd compounds. For the as-prepared silica–Gd–silica particles, their ζ-potential was ca. −13 mV (pH 8.0) that was between those of the silica and the silica–Gd particles. This result indicated that the surface state of the silica–Gd–silica particles was the mixture of the silica and the silica–Gd particles. Isoelectric points of the silica and the silica–Gd particles were ca. 2.5 and ca. 9.0, respectively. The isoelectric point of the silica–Gd–silica particles was ca. 2.5, which was close to that of the silica particles. These results strongly supported the results that perfect silica-coating was observed by the TEM and detected by the EDX analysis.

3.3. MRI properties

Fig. 11 shows T1 weighted images of the silica–Gd and the silica–Gd–silica particles. For comparison, MR signal intensity of water was also estimated. A faint T1 weighted image was

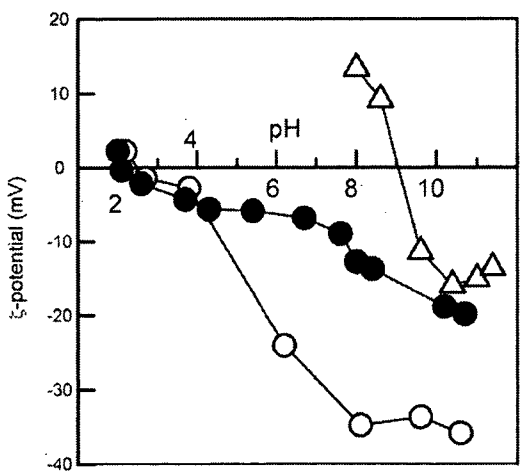

Fig. 10. ζ-Potentials of the silica (○), the silica–Gd (△), and the silica–Gd–silica particles (●).

Please cite this article in press as: Y. Kobayashi et al., Preparation of multilayered silica–Gd–silica core-shell particles and their magnetic resonance images, Colloids Surf. A: Physicochem. Eng. Aspects (2007), doi:10.1016/j.colsurfa.2007.05.024

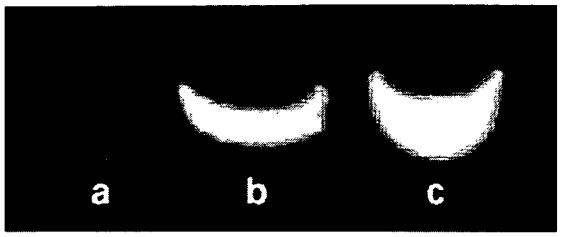

Fig. 11. T1 weighted images of (a) water, (b) silica–Gd and (c) silica–Gd–silica particles. The images were taken with 26 ms for the echo time and 800 ms for the repetition time at a static magnetic field of 0.4 T.

observed in the water. The silica–Gd and the silica–Gd–silica particles exhibited clear images. These results also support that the Gd compounds were well coated on the silica particles, and were not removed during the silica-coating.

4. Summary

A method for producing multilayered silica–Gd–silica core-shell particles has been demonstrated. Silica particles prepared through a modified Stöber method were coated with Gd compounds shells by means of a homogeneous precipitation method. Coating of silica–Gd core-shell particles with silica was achieved by a sol–gel reaction of TEOS initiated by NaOH with the aid of stabilizer PVP. The multilayered particles showed a clear contrast in magnetic resonance imaging. This property for the imaging ability is significantly useful for MRI.

Acknowledgement

This research was partially supported by the Ministry of Education of Japan, Culture, Sports, Science and Technology, a Grant-in-Aid for the COE project, Giant Molecules and Complex Systems and the Center for Interdisciplinary Research of Tohoku University.

References

[1] F. Caruso, A.S. Susha, M. Giersig, H. Möhwald, Magnetic core-shell particles: preparation of magnetite multilayers on polymer latex microspheres, Adv. Mater. 11 (1999) 950–953.
[2] F.G. Aliev, M.A. Correa-Duarte, A. Mamedov, J.W. Ostrander, M. Giersig, L.M. Liz-Marzán, N.A. Kotov, Layer-by-layer assembly of core-shell magnetite nanoparticles: effect of silica coating on interparticle interactions and magnetic properties, Adv. Mater. 11 (1999) 1006–1010.
[3] J.-I. Park, J. Cheon, Synthesis of "solid solution" and "core-shell" type cobalt-platinum magnetic nanoparticles via transmetalation reactions, J. Am. Chem. Soc. 123 (2001) 5743–5746.
[4] M. Wu, Y.D. Zhang, S. Hui, T.D. Xiao, S. Ge, W.A. Hines, J.I. Budnick, Structure and magnetic properties of SiO_2-coated Co nanoparticles, J. Appl. Phys. 92 (2002) 491–495.
[5] Y. Lu, Y. Yin, B.T. Mayers, Y. Xia, Modifying the surface properties of superparamagnetic iron oxide nanoparticles through a sol–gel approach, Nano Lett. 2 (2002) 183–186.
[6] S.M. Marinakos, D.A. Shultz, D.L. Feldheim, Gold nanoparticles as templates for the synthesis of hollow nanometer-sized conductive polymer capsules, Adv. Mater. 11 (1999) 34–37.
[7] G. Oldfield, T. Ung, P. Mulvaney, Au@SnO_2 core-shell nanocapacitors, Adv. Mater. 12 (2000) 1519–1522.
[8] L.Y. Wang, Y.-J. Lin, W.-Y. Chiu, Synthesis and properties of monodisperse conductive core-shell latexes, Synth. Met. 119 (2001) 155–156.
[9] H. Shiho, N. Kawahashi, Preparation of electrically conducting particles consisting of a polymer core and a metallic copper shell, Colloid Polym. Sci. 279 (2001) 1231–1235.
[10] L.M. Liz-Marzán, M. Giersig, P. Mulvaney, Synthesis of nanosized gold-silica core-shell particles, Langmuir 12 (1996) 4329–4335.
[11] M.A. Correa-Duarte, M. Giersig, L.M. Liz-Marzán, Stabilization of CdS semiconductor nanoparticles against photodegradation by a silica coating procedure, Chem. Phys. Lett. 286 (1998) 497–501.
[12] A. Rogach, A. Susha, F. Caruso, G. Sukhorukov, A. Kornowski, S. Kershaw, H. Möhwald, A. Eychmüller, H. Weller, Nano- and microengineering: 3D colloidal photonic crystals prepared from sub-μm-sized polystyrene latex spheres pre-coated with luminescent polyelectrolyte/nanocrystal shells, Adv. Mater. 12 (2000) 333–337.
[13] Y. Kobayashi, M. Horie, M. Konno, B. Rodríguez-González, L.M. Liz-Marzán, Preparation and properties of silica-coated cobalt nanoparticles, J. Phys. Chem. B 107 (2003) 7420–7425.
[14] E. Mine, A. Yamada, Y. Kobayashi, M. Konno, L.M. Liz-Marzán, Direct coating of gold nanoparticles with silica by a seeded polymerization technique, J. Colloid Interf. Sci. 264 (2003) 385–390.
[15] Y. Kobayashi, K. Misawa, M. Kobayashi, M. Takeda, M. Konno, M. Satake, Y. Kawazoe, N. Ohuchi, A. Kasuya, Silica-coating of fluorescent polystyrene microspheres by a seeded polymerization technique and their photo-bleaching property, Colloids Surf. A 242 (2004) 47–52.
[16] S. Gu, J. Onishi, E. Mine, Y. Kobayashi, M. Konno, Preparation of multilayered gold–silica–polystyrene core-shell particles by seeded polymerization, J. Colloid Interf. Sci. 279 (2004) 284–287.
[17] Y. Kobayashi, K. Misawa, M. Takeda, M. Kobayashi, M. Satake, Y. Kawazoe, N. Ohuchi, A. Kasuya, M. Konno, Silica-coating of AgI semiconductor nanoparticles, Colloids Surf. A 251 (2004) 197–201.
[18] Y. Kobayashi, H. Katakami, E. Mine, D. Nagao, M. Konno, L.M. Liz-Marzán, Silica coating of silver nanoparticles using a modified Stöber method, J. Colloid Interf. Sci. 283 (2005) 392–396.
[19] Y. Kobayashi, K. Misawa, M. Kobayashi, M. Takeda, M. Konno, M. Satake, Y. Kawazoe, Noriaki Ohuchi, A. Kasuya, Silica-coating of fluorescent polystyrene microspheres by a modified Stöber method and their stability against photo-bleaching, e-Polymers, no. 052, 2005, pp. 1–8.
[20] E. Mine, M. Hirose, M. Kubo, Y. Kobayashi, D. Nagao, M. Konno, Synthesis of submicron-sized titania-coated silica particles with a sol-gel method and their application to colloidal photonic crystals, J. Sol-Gel Sci. Technol. 38 (2006) 91–95.
[21] Y. Kobayashi, M. Horie, D. Nagao, Y. Ando, T. Miyazaki, M. Konno, Preparation of silica-coated Co–Pt alloy nanoparticles, Mater. Lett. 60 (2006) 2046–2049.
[22] A. Joubert, M.-C. Biston, C. Boudou, J.-L. Ravanat, T. Brochard, A.-M. Charvet, F. Estève, J. Balosso, N. Foray, Irradiation in presence of iodinated contrast agent results in radiosensitization of endothelial cells: consequences for computed tomography therapy, Int. J. Radiat. Oncol. Biol. Phys. 62 (2005) 1486–1496.
[23] V. Comblin, D. Gilsoul, M. Hermann, V. Humblet, V. Jacques, M. Mesbahi, C. Sauvage, J.F. Desreux, Designing new MRI contrast agents: a coordination chemistry challenge, Coord. Chem. Rev. 185–186 (1999) 451–470.
[24] J. Feng, G. Sun, F. Pei, M. Liu, Comparison between GdDTPA and two gadolinium polyoxometalates as potential MRI contrast agents, J. Inorg. Biochem. 92 (2002) 193–199.
[25] Y. Sakurai, M. Takeda, Y. Kawazoe, A. Kasuya, Y. Kobayashi, T. Kamei, M. Nakajima, N. Ohuchi, Nanosized silver-iodide beads as new contrast media for medical application, Breast Dis. 25 (2006) 55–56.
[26] D. Nagao, E. Mine, Y. Kobayashi, M. Konno, Synthesis of silica particles in the hydrolysis of tetraethyl orthosilicate with amine catalysts, J. Chem. Eng. Jpn. 37 (2004) 905–907.

Please cite this article in press as: Y. Kobayashi et al., Preparation of multilayered silica–Gd–silica core-shell particles and their magnetic resonance images, Colloids Surf. A: Physicochem. Eng. Aspects (2007), doi:10.1016/j.colsurfa.2007.05.024

Advanced Materials Research Vols. 29-30 (2007) pp. 191-194
online at http://www.scientific.net
© (2007) Trans Tech Publications, Switzerland
Online available since 2007/11/15

Control of Shell Thickness in Silica-Coating of AgI Nanoparticles

Y. Kobayashi[1,2,a], K. Misawa[1,b], M. Takeda[3,c], N. Ohuchi[3,d], A. Kasuya[4,e] and M. Konno[1,f]

[1]Department of Chemical Engineering, Graduate School of Engineering, Tohoku University, Aoba, Aramaki-aza, Aoba-ku, Sendai 980-8579, Japan

[2]Department of Biomolecular Functional Engineering, Faculty of Engineering, Ibaraki University, 4-12-1 Naka-narusawa-cho, Hitachi, Ibaraki 316-8511, Japan

[3]Division of Surgical Oncology, Graduate School of Medicine, Tohoku University, Seiryo-machi, Aoba-ku, Sendai 980-8574, Japan

[4]Center for Interdisciplinary Research, Tohoku University, Aoba, Aramaki-aza, Aoba-ku, Sendai 980-8578, Japan

[a]ykoba@mx.ibaraki.ac.jp, [b]kiyoto@mickey.che.tohoku.ac.jp, [c]motot@siren.ocn.ne.jp, [d]noriakio@mail.cc.tohoku.ac.jp, [e]kasuya@cir.tohoku.ac.jp, [f]konno@mickey.che.tohoku.ac.jp

Keywords: AgI; Nanoparticle; Core-shell; Silica-coating; Sol-gel; Stöber method

Abstract. Silica-coating of AgI nanoparticles with a Stöber method was carried out to find out reaction conditions for control of the shell thickness. The AgI nanoparticles were prepared from $AgClO_4$ and KI with the use of 3-mercaptopropyltrimethoxysilane (MPS) as a silane coupling agent and dimethylamine (DMA) catalyst for alkoxide hydrolysis. The silica-coating was performed at 4.5×10^{-6}-4.5×10^{-5} M MPS, 11-20 M water, 0.002-0.1 M DMA and 0.005-0.04 M tetraethylorthosilicate at AgI concentrations of 0.1-1 mM. Consequently, AgI-silica core-shell particles could be prepared with the use of 4.5×10^{-5} M MPS, 20 M water, 0.01 M DMA and 1 mM AgI. Silica shell thickness could be varied from 15 to 28 nm with an increase in the TEOS concentration from 0.005 to 0.04 M.

Introduction

Extensive studies on silica-coated nanoparticles have been made [1-10], since the silica-coating provides a greatly enhanced colloidal stability in colloid solution. Our group also performed silica-coating of various particles such as Au [11], Ag [12] and Co [13] with sol-gel methods by applying Stöber method.

AgI has attracted much attention in the field of electronics because of its unique properties such as ionic conductivity and semiconductivity. A study on preparing AgI-silica composite particles was performed by Giersig et al. [14]. They showed that silica-coated Ag nanoparticles were mixed with I_2 solution, in which I_2 molecules diffused in silica shell layer and eventually transformed the Ag to AgI nanoparticles in the inside. However, this method with sodium silicate required long-time, and generated AgI nanoparticles on external silica surface. We have recently developed [15] a technique for silica-coating of AgI nanoparticles applying a coprecipitation from $AgClO_4$ solution and KI solution in combination with the Stöber method. In a preliminary experiment, dispersion stability of AgI nanoparticles during silica-coating was an important factor for producing AgI-silica core-shell (AgI/SiO_2) particles. Taking account of the dispersion stability of AgI nanoparticles, the present work carried out the coating experiments, in which concentrations of a silane coupling agent, water, amine catalyst, alkoxide and AgI nanoparticles were varied to find out reaction conditions suitable for the control of shell thickness.

All rights reserved. No part of contents of this paper may be reproduced or transmitted in any form or by any means without the written permission of the publisher: Trans Tech Publications Ltd, Switzerland, www.ttp.net. (ID: 222.13.35.18-14/12/07,12:14:16)

Experimental

Chemicals. $AgClO_4$ (Kanto Chemical Co., Inc., 99 %) and KI (Wako Pure Chemicals Ltd., 99.5 %) were used as AgI precursors. Tetraethyl orthosilicate (TEOS) (Wako Pure Chemicals Ltd., 95 %), 3-mercaptopropyltrimethoxysilane (MPS) (Aldrich, 97 %) and ethanol (Wako Pure Chemicals Ltd., 99.5 %) were used for silica-coating, and dimethylamine (DMA) (Wako Pure Chemicals Ltd., 50 %) was used as a catalyst for a sol-gel reaction of TEOS and MPS. All chemicals were used as received. Ultrapure deionized water (resistivity higher than 18 MΩ cm) was used in all the preparations.

Preparation of materials. Colloids of AgI nanoparticles were prepared by mixing of $AgClO_4$ and KI solutions at a constant Ag/I molar ratio of 1/2, as follows. A freshly prepared 0.2-2 M $AgClO_4$ aqueous solution (0.015 ml) was added to 0.005-0.05 M KI aqueous solution (6 ml) under vigorous stirring at room temperature to provide AgI concentrations of 0.5×10^{-3}-5×10^{-3} M. Immediately after the mixing, color of the solution turned yellow. Particles prepared at the AgI concentration of 0.5×10^{-3} M were spherical and had an average size of 23.8 nm [20]. In their XRD pattern, peaks were observed at 22.4, 23.7, 25.4, 32.8, 39.2, 42.7 and 46.4 degree. Although these peaks were all attributable to β-AgI [16], all peaks of γ-AgI overlap with the peaks of 002 (23.7 degree), 110 (39.2 degree) and 112 (46.4 degree) of β-AgI. Accordingly, the obtained AgI nanoparticles were β-AgI or a mixture of β-AgI and γ-AgI. The Stöber method with TEOS was applied to silica-coating of the AgI nanoparticles. To the AgI colloid was added an aqueous MPS solution. After 15 min, ethanol and TEOS were successively added to the colloid. Then, the silica-coating was initiated by rapidly injecting an aqueous DMA solution into the AgI/TEOS colloid. Two series of reactions that were different in concentration conditions were examined. In *reaction A*, initial concentrations of $AgClO_4$, KI, MPS and TEOS were ranged keeping the same molar ratio of 1:2:0.045:20 at a given set of the concentrations of 11 M water and 0.01 M DMA. In *reaction B*, initial concentrations of DMA and TEOS were varied from 0.002 to 0.1 M and from 0.005 to 0.04 M, respectively, while initial concentrations of $AgClO_4$, KI and MPS were 1.0×10^{-3}, 2.0×10^{-3} and 4.5×10^{-5} M, respectively, at initial water concentration of 20 M that was high compared with the *reaction A*.

Characterization. The AgI/SiO_2 particles were characterized by transmission electron microscopy (TEM). TEM was performed with a Zeiss LEO 912 OMEGA microscope operating at 100 kV. Samples for TEM were prepared by dropping and evaporating the nanoparticle suspensions on a collodion-coated copper grid. Silica shell thickness was estimated as the difference between AgI particle and composite particle sizes.

Results and Discussion

Silica-coating in *reaction A*. Fig. 1 shows the TEM micrographs of AgI/SiO_2 particles prepared at various concentrations of $AgClO_4$, KI, TEOS and MPS in the *reaction A*. At low AgI concentrations of 0.1×10^{-3}-0.5×10^{-3} M (Figs. 1 (a)–(d)), most of the particles were quasi-perfect core-shells with AgI single core. However, at high AgI concentrations of 0.7×10^{-3} and 1×10^{-3} M (Figs. 1 (e) and (f)), particles with multiple cores were obtained. As the concentrations of $AgClO_4$, KI, TEOS and MPS rise, ionic strength of the solution should increase. Since the increase in ionic strength reduces electrostatic repulsion between the AgI nanoparticles, the reduction of electrostatic repulsion probably promoted the aggregation of AgI nanoparticles. Thus,

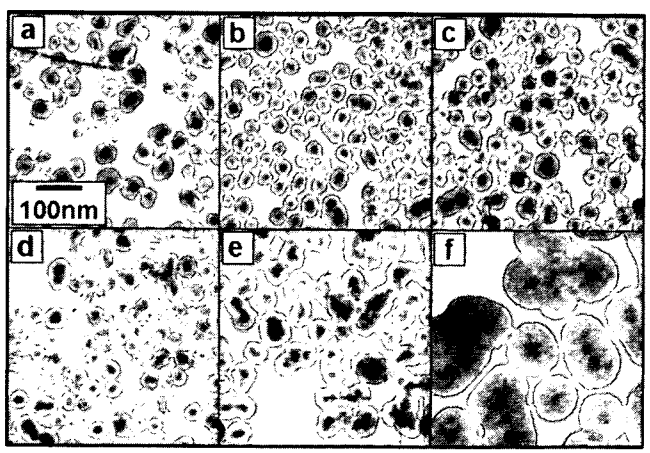

Figure 1. TEM images of AgI/SiO_2 particles. Initial concentrations of $AgClO_4$, KI, MPS and TEOS for the sample (a) were 0.1×10^{-3}, 0.2×10^{-3}, 4.5×10^{-6} and 0.002 M, respectively. For other samples, their concentrations were (b) 2, (c) 3, (d) 5, (e) 7 and 10 times higher than those of the sample (a). Initial concentrations of water and DMA were 11 and 0.01 M with respect to the total solution volume, respectively, in whole samples.